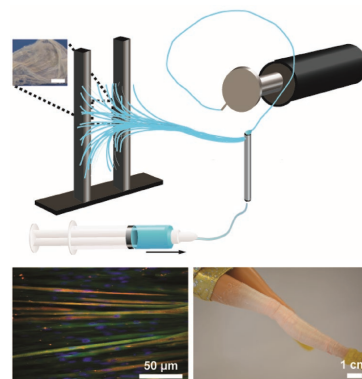


# Design and Fabrication of Fibrous Nanomaterials Using Pull Spinning

Leila F. Deravi, Nina R. Sinatra, Christophe O. Chantre, Alexander P. Nesmith, Hongyan Yuan, Sahm K. Deravi, Josue A. Goss, Luke A. MacQueen, Mohammad R. Badrossamy, Grant M. Gonzalez, Michael D. Phillips, Kevin Kit Parker\*

The assembly of natural and synthetic polymers into fibrous nanomaterials has applications ranging from textiles, tissue engineering, photonics, and catalysis. However, rapid manufacturing of these materials is challenging, as the state of the art in nanofiber assembly remains limited by factors such as solution polarity, production rate, applied electric fields, or temperature. Here, the design and development of a rapid nanofiber manufacturing system termed pull spinning is described. Pull spinning is compact and portable, consisting of a high-speed rotating bristle that dips into a polymer or protein reservoir and pulls a droplet from solution into a nanofiber. When multiple layers of nanofibers are collected, they form a nonwoven network whose composition, orientation, and function can be adapted to multiple applications. The capability of pull spinning to function as a rapid, point-of-use fiber manufacturing platform is demonstrated for both muscle tissue engineering and textile design.



## 1. Introduction

Nanoscale fibers exhibit unique features such as a high surface area-to-volume ratio and tunable stiffness. These characteristics are important design parameters for engineering materials where nano- and microscale topology informs the fabrication of tissue engineering<sup>[1–4]</sup> and drug delivery<sup>[2,5,6]</sup> scaffolds, fabrics,<sup>[7]</sup> filters,<sup>[8]</sup> sensors,<sup>[1,9,10]</sup>

catalysts,<sup>[11,12]</sup> and optical devices.<sup>[13–15]</sup> Such a broad scope of applications demands versatile manufacturing techniques amenable to multiple materials processing and collection conditions. Currently, fiber-fabrication systems can be characterized as melt,<sup>[16–18]</sup> dry,<sup>[19,20]</sup> wet,<sup>[21–23]</sup> or electrospinning<sup>[24,25]</sup>—all of which produce nanofibers using high temperature and pressure (melt, dry, and wet spinning) or electric fields (5–20 kV, electrospinning).<sup>[24–27]</sup> Once formed, the fibers can be collected and processed using external pumps, alternating applied electric fields, spinnerets, coagulation, and wash chambers, or heated drum rolls to form aligned functional materials.<sup>[18,24–26,28,29]</sup> Several electrospinning techniques have been developed to further control fiber deposition and structure, producing aligned fibrous nanostructures by minimizing the distance between a charged nozzle and grounded collector.<sup>[30–35]</sup> While these modifications enable geometries which were previously unattainable for electrospun fibers, the technique remains limited in both speed and the range of materials used. Furthermore, harsh reaction environments,

Prof. L. F. Deravi,<sup>[†]</sup> N. R. Sinatra, C. O. Chantre, Dr. A. P. Nesmith, Prof. H. Yuan, S. K. Deravi, J. A. Goss, Dr. L. A. MacQueen, Dr. M. R. Badrossamy, G. M. Gonzalez, Prof. M. D. Phillips, Prof. K. K. Parker  
Disease Biophysics Group  
Wyss Institute for Biologically Inspired Engineering  
Harvard University  
29 Oxford St. Pierce Hall, Rm 321, Cambridge, MA 02138, USA  
E-mail: kkparker@seas.harvard.edu

<sup>[†]</sup>Present address: Department of Chemistry and Chemical Biology, Northeastern University, Boston, MA 02115, USA

low production rates, and lengthy postprocessing steps, challenge existing systems to rapidly produce point-of-use fibrous materials.

Advanced manufacturing of fiber constructs requires the ability to tune network composition, orientation, and structure under ambient conditions using minimal processing parameters. To meet these demands, techniques incorporating extrusion-based spinning, such as spinneret-based tunable engineered parameters technique (STEP),<sup>[36,37]</sup> rotary jet-spinning (RJS),<sup>[28,38–40]</sup> and touch-spinning<sup>[41]</sup> have emerged as alternatives to the established voltage- or temperature-dependent fiber manufacturing. These systems extrude polymer solutions to form nanofibers either via axial stretching and capillarity (STEP, touch-spinning) or viscous and centrifugal forces (RJS). While STEP and touch-spinning have been optimized to control the deposition and formation of high aspect ratio fibers, they do so at low production rates (550 rpm in STEP and 2500 rpm in touch-spinning). Also, the production of free-standing fibers using these techniques is difficult, as nanofibers are generally suspended along or collected on a fixed substrate. Previously, we developed a rotary jet-spinning system as a high-throughput nanofiber fabrication technique.<sup>[28,38,40,42]</sup> Unlike STEP or touch-spinning, RJS uses a high-speed (up to 75 000 rpm) rotating motor to extrude a nonwoven nanofiber network from a micrometer-sized orifice. This method produces circumferentially aligned fiber networks and is amenable to a range of solvents and materials previously unexplored in fiber manufacturing.<sup>[28,38,40]</sup> However, a portable system is required for point-of-use nanofiber production.

We asked whether we could build a portable nanofiber manufacturing device that enables both high-speed fiber production and precise control of fiber orientation. In this report, we describe the design and utility of a nanofiber fabrication system termed pull spinning, which incorporates a high-speed (up to 45 000 rpm) rotating bristle that pulls a polymer solution from a static droplet to a nanofiber. The dependence of fiber radius and morphology on system parameters such as rotational speed, collector distance, and solution viscosity are investigated. Our data reveal that this technique is capable of rapidly generating both natural and synthetic polymer nanofibers under ambient conditions. Ease of use and functionality are demonstrated for two proof-of-concept applications in muscle tissue engineering and point-of-wear apparel.

## 2. Experimental Section

### 2.1. Materials

Combinations of polymers polycaprolactone ( $M_n$  70 000–90 000; Sigma-Aldrich, St. Louis, MO), gelatin Type A ( $\approx$ 300 bloom; Sigma-Aldrich, St. Louis, MO), polyurethane (McMaster-Carr, Princeton,

NJ), nylon (Nylon 6, Sigma-Aldrich, St. Louis, MO), and solvent 1,1,1,3,3,3-hexafluoro-2-propanol (Sigma-Aldrich, St. Louis, MO) were used in the fiber manufacturing experiments.

### 2.2. Pull Spinning Apparatus

The pull spinning apparatus consists of a high-speed air-powered grinder (McMaster-Carr, Elmhurst, IL) with calibrated speeds up to 45 000 rpm. The pneumatic motor was regulated through a pressure gauge that enabled the direct read-out and calibration of the system under variable pressure. The collector may be, for example, two static posts fixed to a static base board or a rotating cylinder that functions as a spool to collect the fibers projected from the reservoir. The collector was connected to a DeWALT DC 720 1/2" cordless drill driver, operating at 1700 rpm.

### 2.3. Fiber Image Analysis

Varying concentrations of polymers and proteins were spun onto fixed scanning electron microscopy stubs and imaged using a field emission scanning electron microscope (Carl Zeiss, Dresden, Germany). Samples were sputter coated using an Au target (Denton Vacuum, Moorestown, NJ) prior to imaging. All image analysis was done using ImageJ software (National Institutes of Health, Bethesda, MD). Between 150 and 450 fibers were analyzed (4–7 random fields of view per sample, 2–4 samples per condition). Percent beading was calculated by manually identified beads as individual regions of interest (ROIs). The area associated with the identified ROIs was then summed and the collective area was calculated as a function of total fiber area within a field of view. 2D fast Fourier transform (FFT) analysis for nanofiber alignment was measured using the Directionality plug-in for Fiji (<http://fiji.sc/Fiji>, Ashburn, VA), according to previously established methods.<sup>[43,44]</sup> The Directionality plug-in calculates the spatial frequencies within an image given a set of radial directions. The method generated normalized histograms revealing the amount of fibers present between 0° and 180° with a bin size of 1°. Orientation order parameter (OOP) was calculated using a custom MATLAB plugin, according to previous studies.<sup>[45]</sup> A normalized OOP value of 0 represents an isotropic, random fiber network, and a value of 1 indicates a fully aligned, anisotropic fiber sheet.

### 2.4. Viscosity Measurements

Rheological measurements of varying solutions of polycaprolactone (PCL) were recorded using a viscometer (Model AR-G2, TA instruments, New Castle, DE) using a standard-size 40 mm cone and plate geometry. Measured viscosities were derived under steady state shear rates from 0.1 to 1000 s<sup>-1</sup>.

### 2.5. Mechanical Characterization of Fibers

Tensile properties of the fiber samples were measured in air using a uniaxial tension test (Instron 5566 mechanical tester, Norwood, MA). Before each measurement, the thickness, width, and original length of the fiber sample were measured using a micrometer.

## 2.6. Fourier Transform Infrared (FTIR) Spectroscopy

Infrared spectra of nanofiber samples were measured in air using Fourier transform infrared spectroscopy (Bruker Lumos FTIR microscope, Billerica, MA) in attenuated total reflectance (ATR) mode. A resolution of  $4\text{ cm}^{-1}$  and 16 scans was used.

## 2.7. Fabrication of Fiber Muscular Thin Films (fMTF)

fMTFs were fabricated from the following procedure: (1) thin semicured polydimethylsiloxane (PDMS) films were deposited on two ends of a glass coverslip, (2) PCL:gelatin (75:25, 6 wt%/vol%) nanofibers were spun and collected on the coverslip, (3) fMTF cantilevers were cut using a  $\text{CO}_2$  laser prototyping system (Epilog Laser, Golden, CO) with 3% power and 6% speed settings, (4) muscle cells were cultured for a desired time, and finally (5) fMTFs were released and electrically stimulated. Thickness of fMTFs was measured using an optical profiler (Veeco Wyko NT1100, Edina, MN).

## 2.8. fMTF Cell Seeding and Culture

Mouse myoblast cell line (C2C12) (CRL-1772, ATCC, Manassas, VA) were seeded at  $50\,000\text{ cm}^{-2}$  and cultured in a growth medium of Dulbecco's Modified Eagle's Medium (DMEM, 11995-065, GIBCO, Carlsbad, CA) supplemented with 15% fetal bovine serum (Invitrogen, Carlsbad, CA) until confluence. The C2C12s were then cultured for 4 d in an initial differentiation medium consisting of DMEM/F-12 culture medium (12-719F, Lonza, Walkersville, MD) supplemented with 1% horse serum (Gibco, Carlsbad, CA). Next, they were cultured for 6 d in a second differentiation medium consisting of DMEM/F-12 supplemented with 5% horse serum. Only passage numbers from 4 to 15 were used. For the human vascular smooth muscle studies, primary human pulmonary artery vascular smooth muscle cells (Lonza, Walkersville, MD) were cultured for 2 d in M199 culture medium (GIBCO, Carlsbad, CA) supplemented with 10% heat inactivated fetal bovine serum,  $10 \times 10^{-3}\text{ m}$  HEPES (4-(2-hydroxyethyl)-1-piperazineethanesulfonic acid),  $0.1 \times 10^{-3}\text{ m}$  minimum essential medium (MEM) nonessential amino acids,  $20 \times 10^{-3}\text{ m}$  glucose,  $1.5 \times 10^{-6}\text{ m}$  vitamin B-12,  $50\text{ U mL}^{-1}$  penicillin, and  $50\text{ U mL}^{-1}$  streptomycin (GIBCO, Carlsbad, CA). After 2 d, the medium was switched to a serum-free version of the growth media in order to induce a contractile phenotype for 24 h prior to experimentation.

## 2.9. Contractility Assay and Analysis

The contractility assays were performed at desired time points on a stereomicroscope (Model MZ6, Leica Microsystems Inc., Wetzlar, Germany) outside the incubator connected to a National Instruments LabVIEW data acquisition board. A heating platform was set up on the microscope to replicate culture temperature ( $37\text{ }^\circ\text{C}$ ) and electrical stimulation was performed using electrodes immersed in the well, connected to an external field stimulator (Myopacer, IonOptix Corp., Milton, MA). During the contractility experiments, the samples were put in a custom Tyrode's solution developed in the lab ( $1.198\text{ g L}^{-1}$  HEPES,  $0.040\text{ g L}^{-1}$   $\text{NaH}_2\text{PO}_4$ ,  $0.901\text{ g L}^{-1}$  glucose,  $0.265\text{ g L}^{-1}$   $\text{CaCl}_2$ ,  $0.203\text{ g L}^{-1}$   $\text{MgCl}_2$ ,  $0.403\text{ g L}^{-1}$  KCl,  $7.889\text{ g L}^{-1}$

$\text{NaCl}$ , pH 7.4, all chemicals from Sigma-Aldrich, St. Louis, MO). The stimulation was set at high voltage (40 V) to obtain strongest force–frequency curve. For the human vascular smooth muscle, the vasoconstrictors acetylcholine and endothelin (Sigma-Aldrich, St. Louis, MO) were utilized to induce contraction, while the vasodilator HA1077 (Sigma-Aldrich, St. Louis, MO) was used to induce relaxation. Drugs were dosed serially after 10, 20, and 30 min, respectively. To capture the slow contraction of the smooth muscle, images were taken once every 30 s.

## 2.10. fMTF Stress Quantification

The horizontal projections of the cantilevers were tracked using custom ImageJ (NIH, Bethesda, MD) software and the radius of curvature was determined using a custom MATLAB script (Mathworks, Natick, MA). The existing MTF model assumes a cell layer at the surface of the film and calculates the stress derived from the radius of curvature using a modified version of Stoney's equation.<sup>[46,47]</sup> The fMTF model was modified to account for cellular infiltration based on immunostained cryosections.

## 2.11. Immunostaining and Image Analysis

Engineered tissues were fixed using 4% paraformaldehyde (Electron Microscopy Sciences, Hartfield, PA) and 0.5% Triton-X (Sigma-Aldrich, St. Louis, MO) for 5 min. Murine skeletal muscle tissues were labeled with primary antibodies against sarcomeric  $\alpha$ -actinin (Sigma-Aldrich, St. Louis, MO), phalloidin (Life Technologies, Grand Island, NY), and 4',6-diamidino-2-phenylindole (DAPI) (Invitrogen, Carlsbad, CA). Human vascular smooth muscle tissues were stained using phalloidin and DAPI. Immunostained samples were imaged using a Zeiss LSM 510 laser scanning confocal microscope.

## 2.12. Statistical Analysis

All error was reported as standard error of the mean (SEM). Analysis of variance (ANOVA) tests were used during statistical comparisons. For data that were not normally distributed, ANOVA on ranks followed by Dunn's or Tukey's pairwise comparison was used. *P*-values of less than 0.05 were used to measure statistical significance.

# 3. Results and Discussion

## 3.1. Manufacturing Nanofibers Using Pull Spinning

The pull spinning system incorporates two components that work together to initiate nanofiber formation: a fixed polymer reservoir and a rotating bristle attached to a calibrated pneumatic motor (Figure 1a and Figure S1, Supporting Information). When the mandrel is rotated about its axis of symmetry and the bristle is in close proximity ( $\approx 0.050\text{ cm}$ ) to the reservoir, it dips and pulls an ejected polymer droplet into an elongated nanofiber (Movie S1, Supporting Information). High-speed imaging captured during fiber formation suggests four stages: (1) initiation as the bristle contacts the polymer droplet,

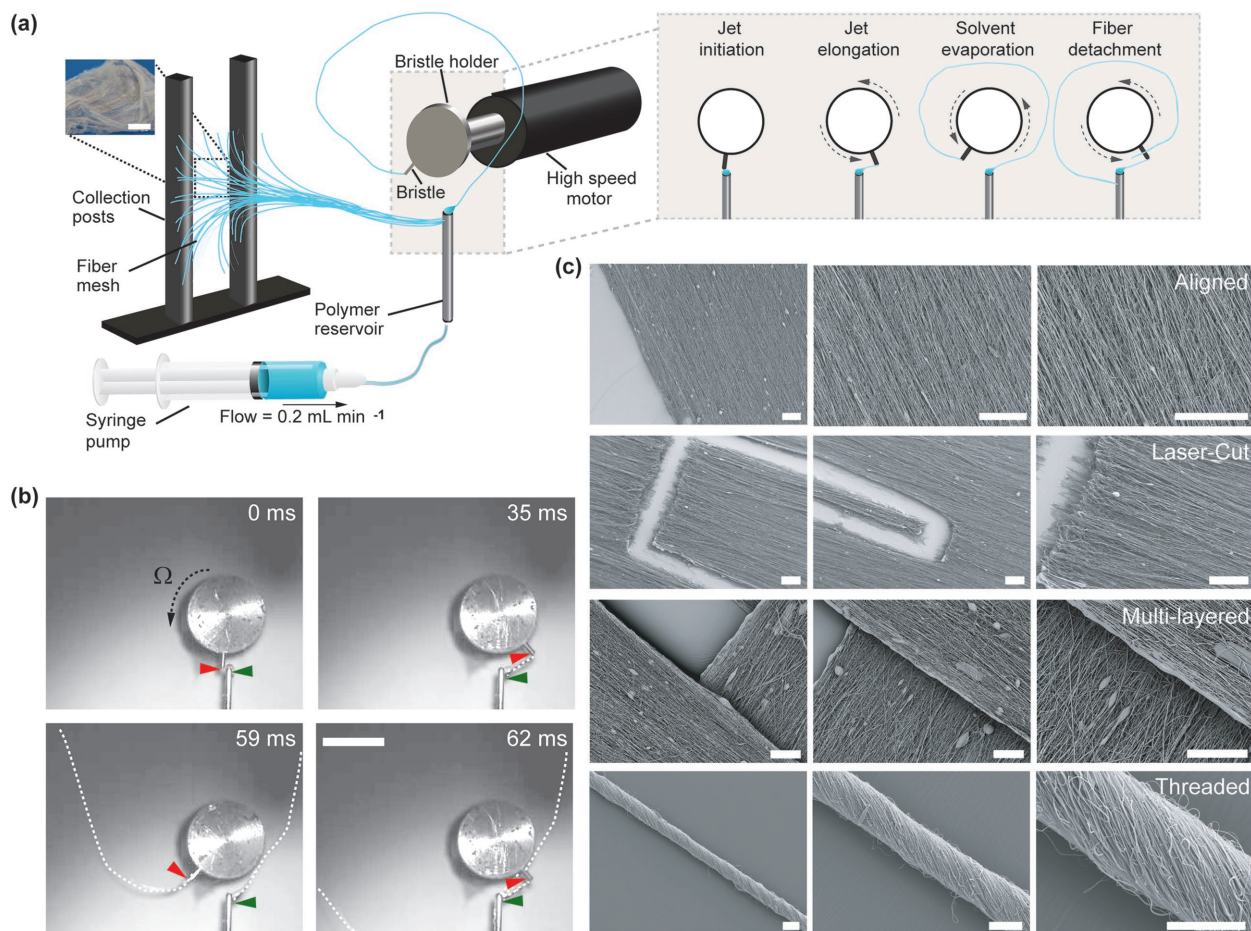


**Figure 1.** Design and function of the pull spinning system. a) Schematic of the pull spinning apparatus with a side view illustration of a fiber being pulled from the polymer reservoir. The pull spinning system consists of a rotating bristle that dips and pulls a polymer jet in a spiral trajectory. Scale bar: 100 mm. b) High-speed images capture the jet initiation as the bristle dips into a polymer droplet, jet elongation as the bristle pulls the droplet, solvent evaporation as the polymer jet solidifies, and fiber detachment from the bristle as the process begins again. The red arrow denotes the location of the bristle/fiber interface, the green arrow represents the location of the nozzle, and the dashed white line denotes a fiber formed throughout one revolution. Scale bar: 1 mm. c) Scanning electron microscopy images of various 6 wt%/vol% PCL:gelatin (3:1) scaffold structures and fiber alignments: aligned sheets (scale bars: 100  $\mu\text{m}$ ), laser cut cantilevers (scale bars: 200  $\mu\text{m}$ ), multilayered woven configurations (scale bars: 50  $\mu\text{m}$ ), and threads (scale bars: 50  $\mu\text{m}$ ).

(2) elongation when the bristle pulls the polymer droplet into a jet, (3) solvent evaporation as the fiber solidifies during one revolution, and (4) detachment of the fiber from the bristle (Figure 1a,b). When the bristle is rotated at an angular speed ( $\Omega$ ) of 45 000 rpm, a polymer jet forms within 35 ms (Figure 1b). The extension of the jet as it is pulled by the rotating bristle is the most crucial stage of the process, without which fiber formation cannot be completed. This jet travels around the bristle holder in a spiral trajectory until one rotation is complete at 60 ms. Both ends of the fiber detach from the bristle at 60 ms as it draws a new droplet from the reservoir. The leading end of the fiber attaches to the reservoir below the droplet, while the trailing end continues rotating around the bristle holder until it travels toward the collector (Figure 1a,b and Movie S2, Supporting Information). The resulting fibers can be collected across static posts or directly onto glass

coverslips as aligned or threaded scaffolds, laser cut into custom configurations, or assembled as woven multilayered structures, illustrating the versatility of fibers generated using this process (Figure 1c).

The pull spinning apparatus consists of a bristle (length 0.531 cm, diameter 0.1 cm) that is fixed perpendicularly onto a rotating disk (radius 0.877 cm,  $S_0$ , Figure 2a). An external syringe pump fills the polymer reservoir at a constant rate of 0.2 mL min<sup>-1</sup>. In this configuration, three variables dominate nanofiber formation: collector distance ( $R_c$ ), angular speed of the bristle ( $\Omega$ ), and kinematic viscosity of the polymer solution ( $\nu$ ). We asked how these system parameters influence fiber radius ( $r$ ) and morphology (% beading). First,  $R_c$  was varied on a log<sub>2</sub> scale from 4 to 16 cm using a 6 wt%/vol% PCL solution in hexafluoro-2-propanol (HFIP), and fiber radius was measured at a constant  $\Omega$  of 45 000 rpm (Figure 2b). Next,

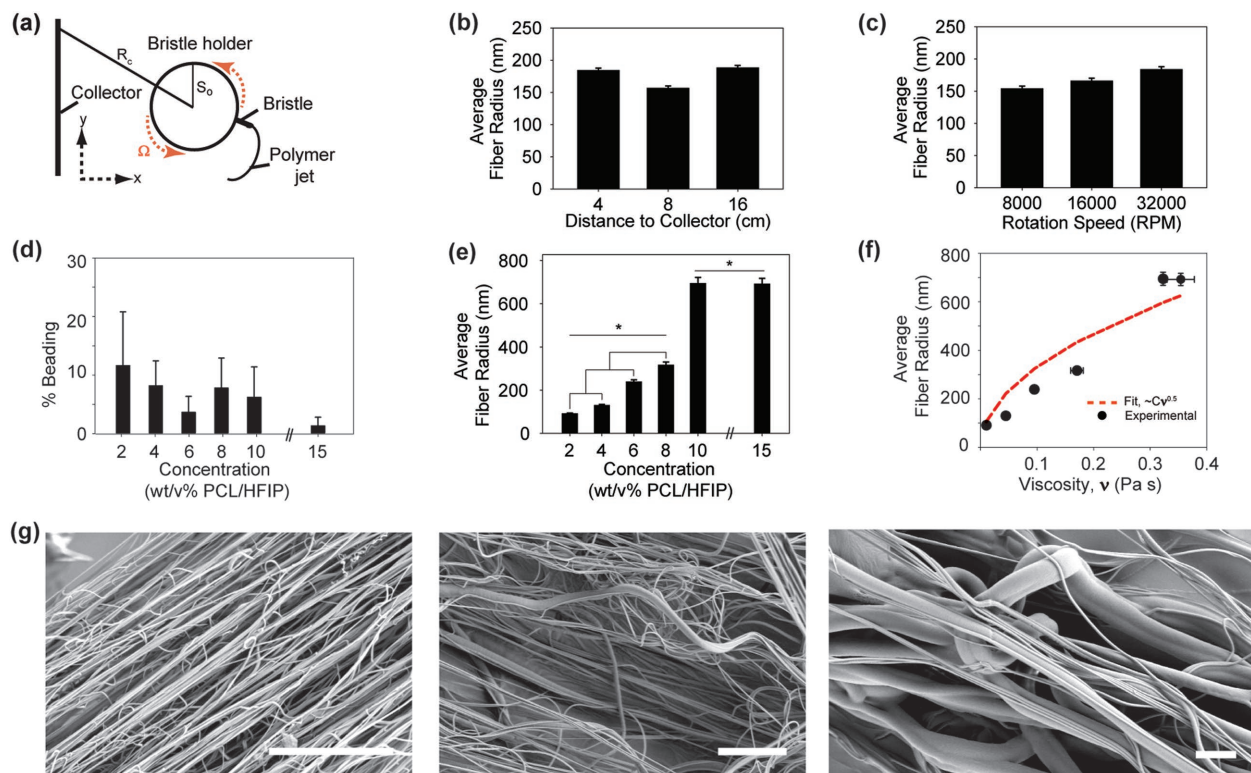


**Figure 2.** Characterizing structural properties of pull spun nanofibers and manufacturing system parameters. a) Side view of fiber being pulled using bristle rotating at speed  $\Omega$ .  $R_c$  is collector distance ( $\approx 10$  cm), and  $S_0$  is the radius (0.877 cm) of the bristle holder. b) Radius of 6 wt%/vol% PCL fibers measured as a function of the distance to the collector (cm). Fibers were produced at a constant  $\Omega$  of 45 000 rpm. c) Radius of 6 wt%/vol% PCL fibers measured as a function of the motor rotation speed (rpm). Fibers were spun at a constant  $R_c$  of 10 cm. d) Percent beading as a function of concentration of PCL in HFIP. e) Fiber radius as a function of polymer concentration. f) Identifying system parameters with varying concentrations of PCL in HFIP (2–15 wt%/vol%). Fiber radius measured as a function of viscosity and best fit by  $\approx Cv^{1/2}$ , where  $C = 1050.4 \text{ m}^2 \text{ s}^{-1}$ . g) Scanning electron images of nanofibers from PCL spun at 2 wt%/vol% in HFIP, 6 wt%/vol% in HFIP, and 15 wt%/vol% HFIP, respectively. Scale bars: 1000 nm. In all graphs,  $N$  is at least 200 fibers across four samples for each condition. Error reported as SEM. \* indicates  $p < 0.05$ .

$\Omega$  was varied on a  $\log_2$  scale from 8000 to 32 000 rpm using the same 6 wt%/vol% PCL solution at fixed  $R_c$  of 10 cm (Figure 2c). We observe no significant differences in fiber radii under the various conditions, suggesting minimal dependence of fiber radius on collector distance and rotational speed within the specified ranges. The experiments were repeated using a 10 wt%/vol% nylon-6 solution in HFIP, and the same trend was observed (Figure S2, Supporting Information). Solution viscosity of PCL was varied, and fiber radius was measured at constant  $R_c$  of 10 cm and  $\Omega$  of 45 000 rpm (Figure 2d,e). We observed that fiber radius increases significantly as a function of polymer concentration (Figure 2e). In spite of these trends, fibers exhibited less than 20% surface defects as evidenced by % beading along the fibers (Figure 2d). These findings were independent of collection time or polymer composition. We observed no significant changes in average fiber radius or % beading in 6 wt%/vol% PCL nanofiber samples collected after 1, 5, or 10 min of continuous fabrication (Figure S3a,b, Supporting Information). Examination of nanofibers fabricated from a 6 wt%/vol% solution of PCL,

polyurethane, or nylon further revealed fiber morphology to be smooth and uniform, without visible pores or defects at the sub-micrometer scale (Figure S4a–c, Supporting Information). Collectively, these data suggest that while increasing solution concentration significantly increases fiber radius, variations in rotational speed, collector distance, or collection time do not over the ranges we tested.

### 3.2. Mechanism behind Fiber Formation

A previously reported scaling law describing jet extension using the RJS system elucidated how fiber formation is governed by a balance between viscous and centrifugal forces, where fiber radius scales with kinematic viscosity. Equation (1) describes this relation as<sup>[38]</sup>

$$r \sim \frac{aU^{\frac{1}{2}}v^{\frac{1}{2}}}{R_c^{\frac{3}{2}}\Omega} \quad (1)$$

In this expression,  $a$  is the initial jet radius,  $U$  represents the angular jet velocity,  $v$  is the kinematic viscosity of the

solution,  $R_c$  is the collector distance, and  $\Omega$  represents the angular speed of the RJS polymer reservoir. We asked whether similar parameters can be applied to describe the pull spinning process. Pull spinning propels a polymer jet in a linear trajectory from a reservoir to a collector. Under these conditions,  $a$ ,  $U$ ,  $R_c$ , and  $\Omega$  are fixed parameters. However, the reservoir is static, unlike the rotating one used in RJS. In this configuration, the jet is pulled and projected toward one primary direction, and fiber formation occurs within a narrow time frame as centrifugal force is applied (0–60 ms at  $\Omega = 45\,000$  rpm). In this time scale, centrifugal force is proportional to the bristle radius but vanishes beyond one rotation cycle because the fiber detaches from the bristle (Figure 1a,b and Movie S1, Supporting Information). This suggests that the fiber thinning process ceases before the nanofiber is projected toward the collector. Experimentally, we observed that the maximum collector distance at which 6 wt%/vol% PCL nanofibers could be spun was 29 cm. ANOVA indicated that the average radius of these fibers ( $125.01 \pm 7.22$  nm) was not statistically different from that of fibers tested at closer ranges (Figure 2b). Thus, the distance between pull spinner and collector has a negligible effect on fiber radius for the given polymer concentration (Figure 2b).

Increasing solidification speed has been shown to increase fiber radius and to mitigate bead formation in the RJS system.<sup>[39]</sup> The use of a pneumatic motor in the pull spinning system introduces an external airflow to facilitate the fiber solidification process. Increasing angular velocity of the bristle results in two competing effects: a larger centrifugal force that accelerates fiber thinning and a higher airflow that hastens fiber solidification rates, thus slowing fiber thinning. These two processes cancel each other, and the change in fiber radius as a function of angular speed is negligibly small, even as  $\Omega$  increases fourfold (Figure 2c). One factor that does directly correlate with fiber radius is solution viscosity, which reduces the rate of fiber thinning and increases with polymer concentration (Figure S5, Supporting Information and Figure 2e). The scaling relation between the fiber radius and the kinematic viscosity has been derived in the previous model for the RJS system as  $r = C \nu^{1/2}$ , where  $C$  is a dimensional constant with units of ( $\text{m}^2 \text{s}^{-1}$ ).<sup>[38]</sup> The constant  $C$  for the pull spinning system can be fit from the experimental relation between radius and viscosity (Figure 2f and Figure S5, Supporting Information), demonstrating that increasing solution viscosities contribute to larger nanofiber radii (Figure 2g) reported within the specified range.

### 3.3. Quantifying Anisotropy of Pull Spun Nanofibers

Point-of-use fiber production for biomedical and textile applications requires the capability to control nanofiber

orientation. Previous force spinning methods utilized centrifugal force to regulate fiber orientation and anisotropy.<sup>[40]</sup> Electrospinning techniques decrease jet instability and control deposition by adjusting the electrode setup, collecting fibers between fixed plates, or minimizing distance between spinneret and collector.<sup>[31,48–50]</sup> However, significant decreases in throughput or disruption of fiber morphology can occur due to residual charge buildup, low collection speed, insufficient solvent evaporation, applied voltage, or polymer flow rate.<sup>[35,50,51]</sup> A comparison of these techniques, along with other nanofiber fabrication systems, is further summarized in Table 1.

We asked whether pull spinning is capable of generating free-standing anisotropic nanofibers in the absence of an underlying substrate or rotational collector. PCL nanofibers of various concentrations (6, 8, and 10 wt%/vol% in HFIP) were collected in air at a distance of 10 cm from the bristle. Network fiber anisotropy was quantified by calculating OOP using a custom MATLAB script; OOP is a normalized parameter, in which 0 represents an isotropic network and 1 indicates a fully aligned sheet.<sup>[45,47]</sup> Nanofibers of all three polymer concentrations displayed OOP values above 0.96, indicating the formation of free-standing, highly aligned nanofiber networks (Figure S2, Supporting Information). While certain near-field<sup>[30,52,53]</sup> or capillary force-based<sup>[36,37,41]</sup> fiber manufacturing methods also provide control of nanofiber spacing and deposition, pull spinning generates highly aligned fiber scaffolds with increased throughput and scalability (details listed in Table 1). Although the production rate of pull spun nanofibers ( $0.15 \text{ g h}^{-1}$  for 6 wt%/vol% PCL/HFIP) does not equal that of previously established gyrotory ( $6000 \text{ g h}^{-1}$ )<sup>[54,55]</sup> or centrifugal force-based ( $60 \text{ g h}^{-1}$ )<sup>[28,56]</sup> methods, fibers produced using this technique demonstrate greater alignment. Thus, pull spinning represents a balance between fiber production rate and precise control of fiber anisotropy.

### 3.4. Fiber Muscular Thin Films Support Contractility Measurements

Given the capability of the pull spinning system to rapidly manufacture anisotropic fiber scaffolds, we asked whether these fibers could be used to build a functional in vitro contractility assay to direct muscle formation and to support function of smooth and skeletal muscle. Previously reported MTFs have demonstrated the ability to model the structural and functional changes that occur in cardiomyopathy and allergic asthma, using hiPSCs and human-derived primary airway smooth muscle, respectively, and expand capabilities for drug evaluation.<sup>[47,57,58]</sup> However, these models are limited to formation of monolayer tissues on 2D polymeric thin films. Quantification of skeletal muscle contractility on a biomimetic nanofibrous

**Table 1.** Comparative advantages, limitations, and nanofiber formation mechanisms for several state-of-the-art nanofiber manufacturing processes, including pull spinning, electrospinning (ES), and melt spinning.

Process	Mechanism	Production specifications	Output [g h <sup>-1</sup> ]	Process advantages	Process limitations	Ref.
Pull spinning	Axial, rotational stretching	45 000 rpm	0.15	<ul style="list-style-type: none"> <li>• Portable</li> <li>• Point-of-use fabrication</li> <li>• Amenable to wide range of polymers</li> <li>• High throughput</li> <li>• Control of fiber orientation</li> <li>• Ease-of-use</li> </ul>	<ul style="list-style-type: none"> <li>• Lower throughput than previous force spinning processes</li> </ul>	–
ES	Electric field	<30 kV	0.01–0.1	<ul style="list-style-type: none"> <li>• Amenable to wide range of polymers</li> </ul>	<ul style="list-style-type: none"> <li>• Low throughput</li> <li>• Requires high V power supply</li> <li>• Alignment is not inherent to process; additional tools required</li> </ul>	[31,59–61]
Near field ES	Electric field	0.2–1.8 kV	N/A	<ul style="list-style-type: none"> <li>• Amenable to wide range of polymers</li> <li>• Precise control of fiber alignment and deposition</li> </ul>	<ul style="list-style-type: none"> <li>• Low throughput</li> <li>• Requires high V power supply</li> <li>• Short distance to collector impedes fiber solidification</li> </ul>	[30,52,53]
Rotary jet (force) spinning	Centrifugal force	Up to 75 000 rpm	60	<ul style="list-style-type: none"> <li>• High throughput</li> <li>• Amenable to wide range of polymers</li> <li>• Ease-of-use</li> </ul>	<ul style="list-style-type: none"> <li>• Bench-top system, not easily portable</li> <li>• Fibers formed circumferentially</li> <li>• Requires postprocessing for use as scaffolds</li> </ul>	[28,39,40,56]
STEP	Capillary force	550 rpm	N/A	<ul style="list-style-type: none"> <li>• Performs in air</li> <li>• Formation of high aspect ratio fibers</li> <li>• Precise control over fiber spacing</li> </ul>	<ul style="list-style-type: none"> <li>• Low throughput, based on production rates</li> <li>• Not easily scalable</li> </ul>	[36,37]
Touch spinning	Axial stretching	500–2500 rpm	N/A	<ul style="list-style-type: none"> <li>• Amenable to wide range of polymers</li> <li>• Performs in air</li> <li>• Control of fiber orientation</li> <li>• Ease-of-use</li> </ul>	<ul style="list-style-type: none"> <li>• Low throughput, based on production rates</li> </ul>	[41]
Brush spinning	Axial stretching	3000 rpm	N/A	<ul style="list-style-type: none"> <li>• Performs in air</li> <li>• Control of fiber orientation</li> <li>• Ease-of-use</li> </ul>	<ul style="list-style-type: none"> <li>• Removing sheets from brush may damage loose fibers</li> <li>• Requires postprocessing for use as scaffolds</li> </ul>	[41]

■ Table 1. Continued.

Process	Mechanism	Production specifications	Output [g h <sup>-1</sup> ]	Process advantages	Process limitations	Ref.
Pressurized gyration	Centrifugal force, solution blowing	Up to 35 000 rpm	6000	<ul style="list-style-type: none"> <li>High production rate</li> </ul>	<ul style="list-style-type: none"> <li>Gas pressure contributes to fiber elongation</li> <li>Requires volatile solvents</li> </ul>	[54,55]
Pressurized melt gyration	Centrifugal force, high temperature	Up to 36 000 rpm	N/A	<ul style="list-style-type: none"> <li>Eliminates dependence on volatile solvents</li> <li>Crystalline polymers formed using gyration temperature</li> </ul>	<ul style="list-style-type: none"> <li>Requires high T</li> <li>Unsuitable for biopolymers</li> <li>Limited to microfiber production</li> </ul>	[62]
ES rapid prototyping	Electric field	3.2 kV	N/A	<ul style="list-style-type: none"> <li>Amenable to wide range of polymers</li> <li>Precise control of fiber deposition and orientation</li> </ul>	<ul style="list-style-type: none"> <li>Requires high V power supply</li> <li>Vibration of collector affects fiber morphology</li> <li>Incomplete fiber solidification between layer deposition distorts fiber morphology</li> </ul>	[35]
Centrifugal melt spinning	Centrifugal force, high temperature	11 000–13 630 rpm	N/A	<ul style="list-style-type: none"> <li>Amenable to wide range of polymers</li> <li>Eliminates dependence on volatile solvents</li> </ul>	<ul style="list-style-type: none"> <li>Unsuitable for biopolymers</li> </ul>	[63]
Gas jet nanofibers	Axial stretching, gas blowing	N/A	0.09–8.6	<ul style="list-style-type: none"> <li>Scalable process is amendable to multiple fiber morphologies</li> </ul>	<ul style="list-style-type: none"> <li>Low production rates</li> <li>Requires volatile solvents for nanofiber formation</li> </ul>	[23]
Melt ES	Electric field, high temperature	5–100 kV	12.5	<ul style="list-style-type: none"> <li>Highly uniform and reproducible fiber diameters</li> </ul>	<ul style="list-style-type: none"> <li>Unsuitable for biopolymers</li> <li>Only applicable for nonconductive polymers</li> </ul>	[33,61,64,65]
Direct write melt ES	Electric field, high temperature	Up to 12 kV	N/A	<ul style="list-style-type: none"> <li>Control over fiber deposition and orientation</li> <li>Produces complex multilayered structures</li> </ul>	<ul style="list-style-type: none"> <li>Requires high V power supply</li> <li>Lag between jet and collector speed yields errors over time</li> <li>Unsuitable for biopolymers</li> <li>Limited to microfiber production</li> </ul>	[33]



substrate has not yet been demonstrated. Using the pull spinning system, we built anisotropic scaffolds (OOP, 0.95) composed of 6 wt%/vol% PCL:gelatin (75:25 in HFIP), a polymer:protein biohybrid known to promote proliferation and maturation of muscle tissue.<sup>[40]</sup> The scaffolds, termed fMTFs, were collected on  $22 \times 22 \text{ mm}^2$  glass coverslips, bound to the edges of the coverslip surface with PDMS, and laser engraved into cantilevers. In this configuration, one end of the cantilever remains anchored to the glass coverslip while the other end is free such that muscle contraction elicits film bending (Figure 3a,b). Seeded with a murine myoblast cell line (C2C12), the fMTFs supported myoblast fusion and maturation into functional muscle tissue, enabling measurable dynamic stress values with quantifiable twitch and tetanus curves (Figure 3c–e and Figure S6, Supporting Information). Immunofluorescence staining of  $\alpha$ -actinin further confirmed the contractile phenotype of the engineered muscle tissue (Figure 3d).

Next, we asked whether the fMTFs could also be utilized to quantify the slow, sustained contraction, and relaxation of primary human vascular smooth muscle. Nanofiber scaffolds were seeded with human vascular

smooth muscle and monitored over 4 d in vitro (Figure 3 and Movie S3, Supporting Information). Our results indicated an increase in contractile stress when treated with the known vasoconstrictors acetylcholine and endothelin-1. Additionally, the engineered human vascular smooth muscle relaxed in response to rho kinase inhibitor HA1077 (Figure 3f). Both muscle cell types exhibited an extended morphology, proliferating along the fiber axis (Figure 3d). Collectively, these data demonstrate the ability of pull spinning to manufacture highly anisotropic, biocompatible fibrous scaffolds that recapitulate native muscle structure and function by supporting and directing the formation of engineered smooth and striated muscle.

### 3.5. Nanofiber Anisotropy Influences Material Performance

Having demonstrated the capability of the pull spinning system to produce anisotropic nanofibers for tissue engineering, we asked whether fiber orientation impacts material properties in the context of apparel design. To test

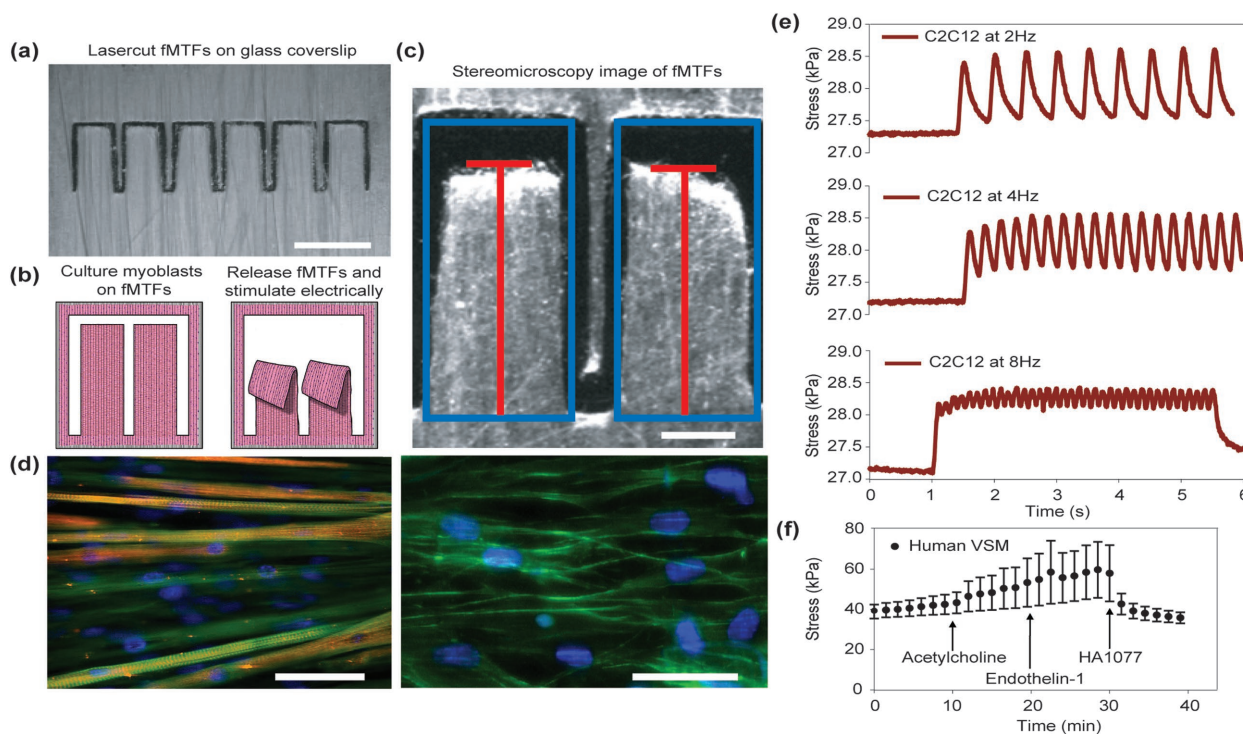


**Figure 3.** Proof-of-concept use of fiber muscular thin films (fMTFs) for in vitro functional testing of muscle tissue. a) Stereomicroscopy image of laser cut 6 wt%/vol% PCL:gelatin (75:25) fMTFs on a glass coverslip. Scale bar: 4 mm. b) Schematic of myoblasts cultured on fMTFs, subsequently released and stimulated electrically. Muscle contraction bends the cantilevers. c) Stereomicroscopy image of fMTF cantilevers. Blue lines indicate fMTF borders prior to their release from the glass coverslip. Horizontal red lines indicate the leading edge positions of the fMTFs during contraction. Scale bar: 500  $\mu\text{m}$ . d) Immunofluorescence staining of murine skeletal muscle (left) and human vascular smooth muscle (right), cultured on fMTFs. Nuclei are stained blue (DAPI) and F-actin is stained green (Phalloidin 488) in both tissues. In murine skeletal muscle tissue,  $\alpha$ -actinin is also stained red. Scale bars: 50  $\mu\text{m}$ . e) Stress readouts from an fMTF cultured for 10 d in DMEM at various pacing frequencies: 2, 4, and 8 Hz. f) Stress trace of human vascular smooth muscle fMTFs serially treated with  $10 \times 10^{-6} \text{ M}$  Acetylcholine after 10 min,  $500 \times 10^{-9} \text{ M}$  Endothelin-1 after 20 min and  $100 \times 10^{-6} \text{ M}$  HA1077 after 30 min.  $N = 1$  chip, 6 films. All errors are reported as SEM.

this, we built nonwoven nanofiber networks composed of 10 wt%/vol% nylon-6, 10 wt%/vol% polyurethane (PU), and a 5:5 wt%/vol% PU:nylon blend along a rotating collector (Figure 4a). Polyurethane and nylon were selected based on their widespread use in performance athletic wear.<sup>[66]</sup> The collector consisted of a drill driver attached to a metal rod terminated by a glass slide. The glass slide permitted continuous collection and facilitated control over fiber orientation, yielding reproducible network thicknesses of  $220 \pm 29 \mu\text{m}$  ( $N = 17$ ). After a 15 min pull-spinning cycle, networks of nonwoven fibers were removed from the mandrel and analyzed using bright field (Figure 4a) and scanning electron microscopy (SEM, Figure 4b). Network isotropy of 5:5 wt%/vol% PU:nylon samples was manually varied by adjusting collection angles to produce anisotropic and crosshatched patterns (Figure 4b). Fiber alignment in the networks was quantified using FFT to measure preferred orientation of structures across multiple fields of view in both  $x$  and  $y$  directions.<sup>[67,68]</sup> FFT is a metric for anisotropy, wherein a histogram with a narrow, unimodal peak represents perfectly aligned fibers, and the abundance or lack of peaks represents a completely isotropic sample. In our

analysis, fibers that are collected as aligned networks have a unimodal histogram; whereas, samples collected in the crosshatched configuration display a bimodal distribution, representing two directions of fiber orientation (Figure 4b). These data suggest that pull spinning onto an adjustable collector at different angles can produce fibrous networks with distinct orientations. Unlike previous electrospinning techniques that have been used to control nanofiber orientation, pull spinning does not require additional devices such as auxiliary<sup>[31]</sup> or parallel<sup>[69]</sup> electrodes, perforated collectors,<sup>[70]</sup> or controlled electrode geometries<sup>[71]</sup> to induce fiber alignment during deposition.

We then asked how fiber orientation and composition affect the bulk mechanical properties of nanofiber networks. Fiber networks were uniaxially loaded at a constant rate of  $8 \text{ mm min}^{-1}$  until failure. The ultimate tensile strength (UTS, Figure 5a) and strain at failure (Figure 5b) for each of the four conditions are reported under tensile load (Figure S7, Supporting Information). 5:5 wt%/vol% PU:nylon was the strongest material tested, exhibiting a UTS of  $2.63 \pm 0.19 \text{ MPa}$  and strain at failure of  $0.73 \pm 0.06$ . The cross-hatched 5:5 wt%/vol% PU:nylon

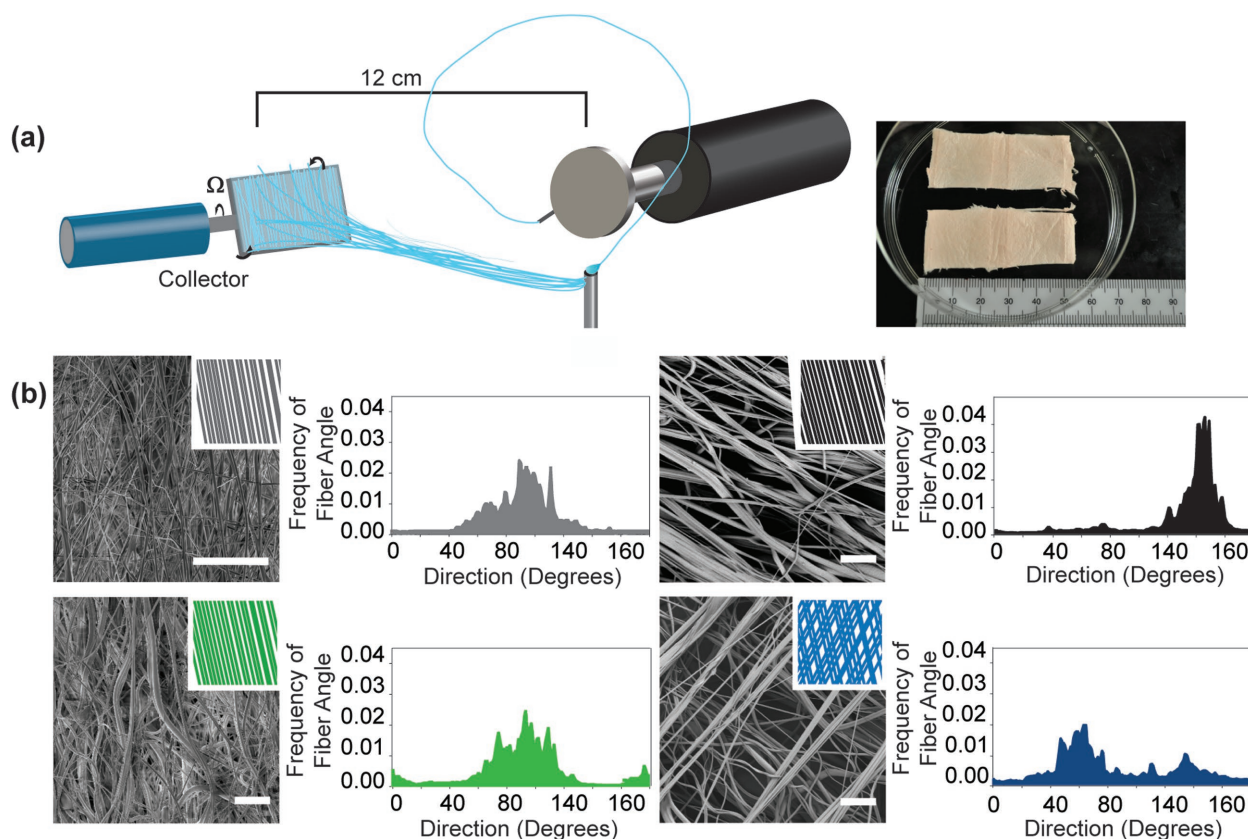


**Figure 4.** Pull spun nanofibers for proof-of-principle apparel design. a) Schematic of collection scheme and sample of 5:5 wt%/vol% polyurethane (PU):nylon (1:1) nanofiber swatches collected after pull spinning. b) Scanning electron images and histograms representing the fiber angle (alignment) as a function of the frequency of the angle of 10 wt%/vol% nylon (gray), 10 wt%/vol% PU (black), 5:5 wt%/vol% anisotropic PU:nylon (green), and 5:5 wt%/vol% PU:nylon crosshatched nanofibers (blue). A multimodal distribution denotes an isotropic mesh, whereas a unimodal distribution indicates uniaxial fiber alignment ( $N = 3\text{--}5$  fields of view over two samples). Scale bar:  $20 \mu\text{m}$ .

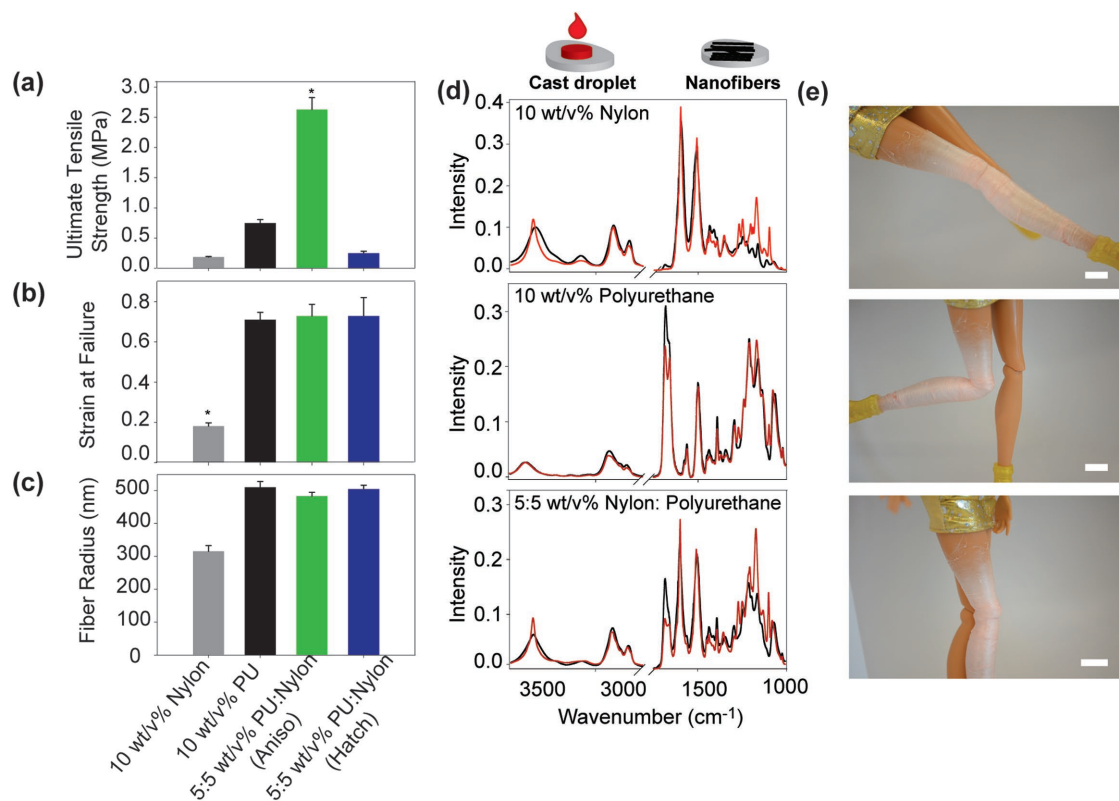


**Figure 5.** a) The ultimate tensile strength and b) strain at failure of each nanofiber network measured under tension. c) Fiber radius measured directly from SEM images ( $N = 200$  fibers over four samples). d) Solution cast polymer films and pull spun nanofibers analyzed using FTIR: 10 w/vol% nylon, 10 w/vol% PU, and 5:5 wt%/vol% PU:nylon films. Red lines represent ATR spectra of drop cast films. Black lines represent ATR spectra of nanofibers collected using pull spinning. In each case, frequency downshifts and broadening of amide I, amide II, and carbonyl vibration modes signify the formation of hydrogen bonds in nylon/PU blend nanofibers. Data are averaged for  $n = 2$  production runs per composition, with four to six FOVs per sample. e) A proof of concept to demonstrate the fabrication of point-of-use apparel using pull spinning. 5:5 wt%/vol% PU:nylon fiber network directly onto the knee joint of a 30 cm doll. Scale bars: 1 cm. All error is reported as SEM. \* indicates  $p < 0.05$ .

nanofabric displayed significantly lower ultimate tensile strength than the anisotropic 5:5 wt%/vol% PU:nylon sample. In contrast, low UTS ( $0.19 \pm 0.01$  MPa) and strain at failure ( $0.18 \pm 0.02$ ) values for the 10 wt%/vol% nylon networks suggest that nylon is the least resistant of the tested networks to mechanical load. The nylon fibers are also the thinnest, with an average radius that is nearly 40% less than that of the other samples (Figure 5c), suggesting that fiber structure and composition may contribute to bulk mechanical properties.

To further understand the role of molecular structure in bulk tensile strength, we used ATR-FTIR spectroscopy to examine the structural changes in the fiber networks as a function of polymer composition (Figure 5d). Characteristic vibration modes of both nylon and PU are evident in the spectra (Table S1, Supporting Information). Our analysis focused on the vibration peaks indicative of hydrogen bond formation—a sign of intrachain bonding. These peaks are represented by amide and carbonyl stretches:  $1637\text{ cm}^{-1}$  (amide I),  $1547\text{ cm}^{-1}$  (amide II),  $1729\text{ cm}^{-1}$  (carbonyl), and  $3300\text{ cm}^{-1}$  (amide). Hydrogen bonding between amide

groups of nylon and urethane linkages of PU increases bulk tensile strength by reducing slippage between the anisotropic polymer chains. The increase in hydrogen bond formation is indicated by amide and carbonyl peak broadening and a downshift of N–H and C=O stretching (Figure 5d, black lines). Overall, the frequency peak positions of the IR data for the three polymer compositions suggest that blending PU and nylon increases hydrogen bonding within the formed fibers. These interactions manifest on the macroscale through stronger tensile strength for the anisotropic 5:5 wt%/vol% PU:nylon blend. These data are compared against drop cast films of similar compositions (Figure 5d, red lines). Comparing the vibration modes of the cast films to those of the polymerized pull spun nanofibers reveals significant increases in hydrogen bonding after pull spinning (Figure 5d), further suggesting the role of this process in forming intrachain bonds.

Collectively, these data suggest that pull spinning can be used to fabricate point-of-use nanofibers whose mechanical performance can be customized according to the composition and structural properties of the starting

material. This capability will enable us to tune fiber performance specific to a final material application.

### 3.6. Point-of-Use Apparel Fabrication

A simple proof-of-principle application of the pull spinning system for apparel was demonstrated using the strongest tested polymer material, the 5:5 wt%/vol% PU:nylon blend, spun directly onto the knee joint of a 30 cm doll (Figure 5e). The knee was selected as an ideal trial area based on its high range of motion and nonuniform topography. We found that the nanofibrous textile conformed to the shape of the joint during pull spinning, demonstrating no delamination following fiber formation. The joint was extended from 0° to 135° through the full range of motion. The rate at which the knee is flexed was varied from 1 to 200 extensions  $\text{min}^{-1}$  (Movie S4, Supporting Information). Regardless of the rate of deformation, the nanofiber network remained intact during joint movement, exhibiting no tearing (Figure 5e). This preliminary trial suggests that pull spinning is a viable fabrication tool for point-of-wear manufacturing.

## 4. Conclusions

We have built a compact nanofiber fabrication system that rapidly generates continuous nonwoven nanofibers independent of external system parameters. Like other well-established techniques, pull spinning works by extruding a polymer or protein droplet into a solid nanofiber that can be collected as single fiber-thick layers or as a multilayered network on a static or rotating substrate. Unlike other processes, pull spinning is a “point-and-shoot” method that facilitates high-speed nanofiber fabrication while maintaining control of fiber orientation ( $\text{OOP} > 0.96$ ) and deposition. In this study, we examined the effect of rotational speed, collection time, collector distance, polymer concentration, and composition on the radius and morphology of pull spun polymer nanofibers. We adapted a scaling law to describe how centrifugal force and kinematic viscosity influence nanofiber formation and nanofiber radius. Of these two parameters, we concluded that the kinematic viscosity of the initial polymer solution governs the radius of the formed fiber. The upper and lower limits for fiber radius were defined by the maximum and minimum solution viscosities of a given polymer for which fiber thinning can occur. Future studies will address the role of other environmental parameters (e.g., humidity, temperature, and solvent volatility) that may similarly influence fiber morphology and production quality.

We also present two proof-of-concept applications for tissue engineering and textile design, illustrating the versatility of the pull spinning system for nanomaterials

manufacturing. In the first case, we show how pull spinning can be used to fabricate fMTFs, a new nanofiber-based platform that can recapitulate the anisotropy and nanostructure of skeletal and smooth muscle tissue. We show that fMTFs support functional measurement of twitch and tetanus curves (murine skeletal muscle) and changes in contractile stress in response to vasoconstrictors and a rho kinase inhibitor (human vascular smooth muscle). In a separate study, we demonstrate that the pull spinning system can be adapted to point-of-wear apparel. We show how nanofibrous textiles can be spun directly onto the knee joint of a doll without delamination as the joint was flexed and relaxed over multiple cycles. This simple, proof-of-concept study demonstrates the utility of this system for point-of-use textile manufacturing. Future applications for directed production of customizable nanotextiles could extend to spray-on sportswear that gradually heats or cools an athlete's body, sterile bandages deposited directly onto a wound, and fabrics with locally varying mechanical properties.

## Supporting Information

Supporting Information is available from the Wiley Online Library or from the author.

**Acknowledgements:** L.F.D. and N.R.S. contributed equally to this work and are co-first authors. The authors gratefully acknowledge the Wyss Institute for Biologically Inspired Engineering and the Harvard John A. Paulson School of Engineering and Applied Sciences. This work was performed in part at the Center for Nanoscale Systems (CNS), a member of the National Nanotechnology Infrastructure Network (NNIN), which was supported by the National Science Foundation under NSF Award No. ECS-0335765. This work also received funding from the Harvard University Materials Research Science and Engineering Center under the National Science Foundation (Award No. DMR-1420570), from the National Center for Advancing Translational Sciences of the National Institutes of Health (Award No. UH3TR000522), from the Defense Advanced Research Project Agency (DARPA) under Cooperative Agreement No. W911NF-12-2-0036, and from Sanofi (Award No. 214565). The views and conclusions contained in this document are those of the authors and should not be interpreted as representing the official policies, either expressed or implied, of the Defense Advanced Research Projects Agency, or of the U.S. Government. The authors also acknowledge Ali Deitch, and students and faculty of the United States Military Academy, West Point, NY: Calla Glavin, Virginia Phillips, Derek West, Anna Lan, Margaret Churchill, Andrew Dumont, and Kris Ahlers for their contributions to the preliminary studies in this work. The authors appreciate the assistance of Dr. Andrew Magyar with optical profilometry measurements, the graphic artwork provided by Karaghen Hudson, and the helpful comments of Dr. Johan Lind and Dr. Thomas Grevesse.

Received: September 20, 2016; Revised: December 2, 2016;  
Published online: ; DOI: 10.1002/mame.201600404

Keywords: nanofiber; nanotechnology; point-of-use; pull spinning; tissue engineering

- [1] J. S. Lee, O. S. Kwon, S. J. Park, E. Y. Park, S. A. You, H. Yoon, J. Jang, *ACS Nano* **2011**, *5*, 7992.
- [2] A. Sharma, A. Gupta, G. Rath, A. Goyal, R. B. Mathur, S. R. Dhakate, *J. Mater. Chem. B* **2013**, *1*, 3410.
- [3] W. Liu, S. Thomopoulos, Y. Xia, *Adv. Healthcare Mater.* **2012**, *1*, 10.
- [4] G. A. Silva, C. Czeisler, K. L. Niece, E. Beniash, D. A. Harrington, J. A. Kessler, S. I. Stupp, *Science* **2004**, *303*, 1352.
- [5] M. Ignatova, N. Manolova, I. Rashkov, *Macromol. Biosci.* **2013**, *13*, 860.
- [6] T. J. Sill, H. A. von Recum, *Biomaterials* **2008**, *29*, 1989.
- [7] L. F. Deravi, H. M. Golecki, K. K. Parker, *J. Chem. Biol. Interfaces* **2013**, *1*, 25.
- [8] L. Matlock-Colangelo, D. Cho, C. L. Pitner, M. W. Frey, A. J. Baeumner, *Lab Chip* **2012**, *12*, 1696.
- [9] Z. C. Sun, E. Zussman, A. L. Yarin, J. H. Wendorff, A. Greiner, *Adv. Mater.* **2003**, *15*, 1929.
- [10] T. Zhang, W. Wang, D. Zhang, X. Zhang, Y. Ma, Y. Zhou, L. Qi, *Adv. Funct. Mater.* **2010**, *20*, 1152.
- [11] Z. Zhang, C. Shao, X. Li, C. Wang, M. Zhang, Y. Liu, *ACS Appl. Mater. Interfaces* **2010**, *2*, 2915.
- [12] Y. Dai, W. Liu, E. Formo, Y. Sun, Y. Xia, *Polym. Adv. Technol.* **2011**, *22*, 326.
- [13] Y. Ishii, R. Kaminose, M. Fukuda, *J. Phys.: Conf. Ser.* **2013**, *433*, 012006.
- [14] J. Kim, J. Noh, S. Jo, K. E. Park, W. H. Park, T. S. Lee, *ACS Appl. Mater. Interfaces* **2013**, *5*, 6038.
- [15] A. Camposeo, L. Persano, D. Pisignano, *Macromol. Mater. Eng.* **2013**, *298*, 487.
- [16] K. Mezghani, J. E. Spruiell, *J. Polym. Sci., Part B: Polym. Phys.* **1998**, *36*, 1005.
- [17] K. P. Matabola, A. R. De Vries, F. S. Moolman, A. S. Luyt, *J. Mater. Sci.* **2009**, *44*, 6213.
- [18] A. M. Jordan, L. T. Korley, *Macromolecules* **2015**, *48*, 2614.
- [19] S. M. Berry, S. A. Harfenist, R. W. Cohn, R. S. Keynton, *J. Micromech. Microeng.* **2006**, *16*, 1825.
- [20] W. Wei, Y. P. Zhang, Y. M. Zhao, J. Luo, H. L. Shao, X. C. Hu, *Mater. Sci. Eng., C* **2011**, *31*, 1602.
- [21] D. M. Phillips, L. F. Drummy, R. R. Naik, H. C. De Long, D. M. Fox, P. C. Trulove, R. A. Mantz, *J. Mater. Chem.* **2005**, *15*, 4206.
- [22] K. D. Nelson, A. Romero, P. Waggoner, B. Crow, A. Borneman, G. M. Smith, *Tissue Eng.* **2003**, *9*, 1323.
- [23] R. E. Benavides, S. C. Jana, D. H. Reneker, *ACS Macro Lett.* **2012**, *1*, 1032.
- [24] Z. M. Huang, Y. Z. Zhang, M. Kotaki, S. Ramakrishna, *Compos. Sci. Technol.* **2003**, *63*, 2223.
- [25] Q. P. Pham, U. Sharma, A. G. Mikos, *Tissue Eng.* **2006**, *12*, 1197.
- [26] C. J. Luo, S. D. Stoyanov, E. Stride, E. Pelan, M. Edirisinghe, *Chem. Soc. Rev.* **2012**, *41*, 4708.
- [27] D. H. Reneker, A. L. Yarin, *Polymer* **2008**, *49*, 2387.
- [28] M. R. Badrossamay, H. A. McIlwee, J. A. Goss, K. K. Parker, *Nano Lett.* **2010**, *10*, 2257.
- [29] C. Lawson, A. Stanishevsky, M. Sivan, P. Pokorny, D. Lukáš, *J. Appl. Polym. Sci.* **2016**, *133*, app.43232.
- [30] D. Sun, C. Chang, S. Li, L. Lin, *Nano Lett.* **2006**, *6*, 839.
- [31] M. M. Arras, C. Grasl, H. Bergmeister, H. Schima, *Sci. Technol. Adv. Mater.* **2016**, *13*, 035008.
- [32] D. W. Hutmacher, P. D. Dalton, *Chem. - Asian J.* **2011**, *6*, 44.
- [33] T. D. Brown, P. D. Dalton, D. W. Hutmacher, *Adv. Mater.* **2011**, *23*, 5651.
- [34] C. Song, J. A. Rogers, J.-M. Kim, H. Ahn, *Macromol. Res.* **2015**, *23*, 118.
- [35] A. Chanthakulchan, P. Koomsap, K. Auysan, P. Supaphol, *Rapid Prototyping J.* **2015**, *21*, 329.
- [36] A. S. Nain, M. Sitti, A. Jacobson, T. Kowalewski, C. Amon, *Macromol. Rapid Commun.* **2009**, *30*, 1406.
- [37] A. S. Nain, J. A. Phillippi, M. Sitti, J. MacKrell, P. G. Campbell, C. Amon, *Small* **2008**, *4*, 1153.
- [38] P. Mellado, H. A. McIlwee, M. R. Badrossamay, J. A. Goss, L. Mahadevan, K. K. Parker, *Appl. Phys. Lett.* **2011**, *99*, 203107.
- [39] H. M. Golecki, H. Yuan, C. Glavin, B. Potter, M. R. Badrossamay, J. A. Goss, M. D. Phillips, K. K. Parker, *Langmuir* **2014**, *30*, 13369.
- [40] M. R. Badrossamay, K. Balachandran, A. K. Capulli, H. M. Golecki, A. Agarwal, J. A. Goss, H. Kim, K. Shin, K. K. Parker, *Biomaterials* **2014**, *35*, 3188.
- [41] A. Tokarev, D. Asheghali, I. M. Griffiths, O. Trotsenko, A. Gruz, X. Lin, H. A. Stone, S. Minko, *Adv. Mater.* **2015**, *27*, 6526.
- [42] T. B. Mindru, L. Ignat, I. B. Mindru, M. Pinteala, *Fibers Polym.* **2013**, *14*, 1526.
- [43] I. Hamley, *Introduction to Soft Matter: Polymers, Colloids, Amphiphiles and Liquid Crystals*, John Wiley & Sons Ltd, Chichester, UK **2000**.
- [44] J. Schindelin, I. Arganda-Carreras, E. Frise, V. Kaynig, M. Longair, T. Pietzsch, S. Preibisch, C. Rueden, S. Saalfeld, B. Schmid, *Nat. Methods* **2012**, *9*, 676.
- [45] D. Volfson, S. Cookson, J. Hasty, L. S. Tsimring, *Proc. Natl. Acad. Sci. USA* **2008**, *105*, 15346.
- [46] G. Wang, M. L. McCain, L. Yang, A. He, F. S. Pasqualini, A. Agarwal, H. Yuan, D. Jiang, D. Zhang, L. Zangi, J. Geva, A. E. Roberts, Q. Ma, J. Ding, J. Chen, D. Z. Wang, K. Li, J. Wang, R. J. Wanders, W. Kulik, F. M. Vaz, M. A. Laflamme, C. E. Murry, K. R. Chien, R. I. Kelley, G. M. Church, K. K. Parker, W. T. Pu, *Nat. Med.* **2014**, *20*, 616.
- [47] A. P. Nesmith, A. Agarwal, M. L. McCain, K. K. Parker, *Lab Chip* **2014**, *14*, 3925.
- [48] S. K. Vimal, N. Ahamad, D. S. Katti, *Mater. Sci. Eng., C* **2016**, *63*, 616.
- [49] J. Walser, S. J. Ferguson, *J. Mech. Behav. Biomed. Mater.* **2016**, *58*, 188.
- [50] M. Acharya, G. K. Arumugam, P. A. Heiden, *Macromol. Mater. Eng.* **2008**, *293*, 666.
- [51] I. Teh, F. L. Zhou, P. L. Hubbard Cristinacce, G. J. Parker, J. E. Schneider, *J. Magn. Reson. Imaging* **2015**, *43*, 594.
- [52] G. S. Bisht, G. Canton, A. Mirsepassi, L. Kulinsky, S. Oh, D. Dunn-Rankin, M. J. Madou, *Nano Lett.* **2011**, *11*, 1831.
- [53] T. Lei, X. Lu, F. Yang, *AIP Adv.* **2015**, *5*, 041301.
- [54] S. Mahalingam, M. Edirisinghe, *Macromol. Rapid Commun.* **2013**, *34*, 1134.
- [55] B. T. Raimi-Abraham, S. Mahalingam, M. Edirisinghe, D. Q. Craig, *Mater. Sci. Eng., C* **2014**, *39*, 168.
- [56] K. Sarkar, C. Gomez, S. Zambrano, M. Ramirez, E. de Hoyos, H. Vasquez, K. Lozano, *Mater. Today* **2010**, *13*, 12.
- [57] A. Grosberg, A. P. Nesmith, J. A. Goss, M. D. Brigham, M. L. McCain, K. K. Parker, *J. Pharmacol. Toxicol. Methods* **2012**, *65*, 126.
- [58] A. W. Feinberg, A. Feigel, S. S. Shevkopyas, S. Sheehy, G. M. Whitesides, K. K. Parker, *Science* **2007**, *317*, 1366.

- [59] J. Doshi, D. H. Reneker, "Electrospinning process and applications of electrospun fibers", in *Conf. Record of IEEE Industry Applications Society Annual Meeting*, Toronto, October **1993**.
- [60] N. M. Thoppey, J. R. Bochinski, L. I. Clarke, R. E. Gorga, *Polymer* **2010**, *51*, 4928.
- [61] H. Li, W. Yang, in *Non-woven Fabrics* (Ed: H.-Y. Jeon), InTech, **2016**, p. 33.
- [62] Z. Xu, S. Mahalingam, P. Basnett, B. Raimi-Abraham, I. Roy, D. Craig, M. Edirisinghe, *Macromol. Mater. Eng.* **2016**, *301*, 922.
- [63] T. Huang, L. R. Marshall, J. E. Armantrout, S. Yembrick, W. H. Dunn, J. M. Oconnor, T. Mueller, M. Avgousti, M. D. Wetzel, *E I Du Pont De Nemours And Company, Invs.*, **2012**.
- [64] L. Larrondo, R. St John Manley, *J. Polym. Sci.: Polym. Phys. Ed.* **1981**, *19*, 909.
- [65] H. Li, H. Chen, X. Zhong, W. Wu, Y. Ding, W. Yang, *J. Appl. Polym. Sci.* **2014**, *131*, app.40515.
- [66] R. Liu, T. Little, J. Williams, *Fibers Polym.* **2014**, *15*, 632.
- [67] E. M. M. Manders, F. J. Verbeek, J. A. Aten, *J. Microsc.* **1993**, *169*, 375.
- [68] G. Wang, M. L. McCain, L. Yang, A. He, F. S. Pasqualini, A. Agarwal, H. Yuan, D. Jiang, D. Zhang, L. Zangi, J. Geva, A. E. Roberts, Q. Ma, J. Ding, J. Chen, D. Z. Wang, K. Li, J. Wang, R. J. Wanders, W. Kulik, F. M. Vaz, M. A. Laflamme, C. E. Murry, K. R. Chien, R. I. Kelley, G. M. Church, K. K. Parker, W. T. Pu, *Nat. Med.* **2014**, *20*, 616.
- [69] J. Zhao, H. Liu, L. Xu, *Mater. Des.* **2016**, *90*, 1.
- [70] G. Rakesh, G. Ranjit, K. Karthikeyan, P. Radhakrishnan, P. Biji, *eXPRESS Polym. Lett.* **2015**, *9*, 105.
- [71] J. Stevenson, S. Lattante, P. André, M. Anni, G. Turnbull, *Appl. Phys. Lett.* **2015**, *106*, 173301.